Magnetic resonance of calcified tissues

Felix W. Wehrli *

Laboratory for Structural NMR Imaging, Department of Radiology, Perelman School of Medicine, University of Pennsylvania, United States

ARTICLE INFO

ABSTRACT

MRI of the human body is largely made possible by the favorable relaxation properties of protons of water and triacyl glycerides prevalent in soft tissues. Hard tissues – key among them bone – are generally less amenable to measurement with in vivo MR imaging techniques, not so much as a result of the lower proton density but rather due to the extremely short life-times of the proton signal in water bound to solid-like entities, typically collagen, or being trapped in micro-pores. Either mechanism can enhance T2 relaxation by up to three orders of magnitude relative to their soft-tissue counterparts. Detection of these protons requires solid-state techniques that have emerged in recent years and that promise to add a new dimension to the study of hard tissues. Alternative approaches to probe calcified tissues exploit their characteristic magnetic properties. Bone, teeth and extra-osseous calcium-containing biomaterials are unique in that they are more diamagnetic than all other tissues and thus yield information indirectly by virtue of the induced magnetic fields present in their vicinity. Progress has also been made in methods allowing very high-resolution structural imaging of trabecular and cortical bone relying on detection of the surrounding soft-tissues. This brief review, much of it drawn from work conducted in the author's laboratory, seeks to highlight opportunities with focus on early-stage developments for image-based assessment of structure, function, physiology and mechanics of calcified tissues in humans via liquid and solid-state approaches, including proton, deuteron and phosphorus NMR and MRI.

1. Chemistry, architecture and physiology of bone

Bone is a hierarchically organized biomaterial evolved so as to optimally fulfill its multiple functions ranging from weight-bearing and locomotion to serving as a store for calcium and phosphorus. The major chemical constituents of bone are an organic fraction, consisting predominantly of type-I collagen (~50% by volume), an inorganic or mineral fraction (~35%), made up of poorly mineralized nonstoichiometric calcium hydroxyl apatite with a much smaller and variable fraction of carbonate apatite. The balance is water, with its majority bound to collagen, and a smaller fraction occupying the bone's pore structure. The mineral crystals are interspersed in the gaps between successive collagen fibrils [1]. The bone's compressive strength is largely conferred by the material's inorganic component whereas collagen is responsible for the bone's tensile strength. On a macrostructural level bone is about 80% compact (or cortical) and 20% trabecular. Cortical bone forms the shell encasing bone marrow and blood vessels, dominating the shaft of the extremities and femoral neck whereas trabecular bone, consisting of a meshwork on interconnected plates and rods, is dominant in the vertebrae, ribs and near the joints where stresses are multidirectional and tensile and torsional loading occurs.

Bone is a living tissue with its own blood supply and ability for self-repair through a process called 'remodeling', referring to the interplay of two types of cells: osteoblasts, the bone-forming, and osteoclasts, the bone-resorbing cells. A third type of cells, the osteocytes occupying small cavities on the order of 30 μm in diameter, act as pressure transducers providing signals to osteoblast to induce bone formation. Osteocytes are interconnected with each other through a system of channels, called canaliculi, about 100 nm in diameter. Cortical bone further is permeated by a network of channels, on the order of 50–100 μm in diameter, carrying blood vessels, in contrast to the blood supply to trabecular bone, which is effected through the marrow's microvascular system.

2. Indirect detection of trabecular and cortical bone microstructure

We refer to 'indirect detection' of microarchitecture methods that obviate the need for resolving individual trabecular elements (which are on the order of 100 μm thickness) in trabecular bone or, for example, pore volume fraction in cortical bone (with pore diameters ranging from 10 to several hundred micrometers), thereby obviating the need to resolve individual structural elements. Such approaches entail significant advantages in terms of signal-to-noise (SNR) requirements.

* Fax: +1 215 662 7263.
  E-mail address: wehrli@mail.med.upenn.edu

3. Methods exploiting internal magnetic fields for the study of trabecular bone architecture

3.1. Static dephasing regime

The majority of low-resolution MRI studies of bone architecture exploit the bone's diamagnetic properties. The greater density of higher atomic-number elements in bone mineral (notably calcium and phosphorus) render bone tissue considerably more diamagnetic than bone marrow (by about 3 ppm, S.I.) [2]. Compartmentalization of the two phases (i.e. bone and marrow) leads to induced inhomogeneous magnetic fields near the interface of the two phases [3].

The empirical observation of a rapid decay of the trabecular bone marrow FID or gradient echo thus results from local induced field gradients (also referred to 'internal magnetic field gradients' IMFG). The signal $S(t)$ in the presence of a mesoscopic perturber such as a trabecula in a small volume element as, for example, an imaging voxel can be written as

$$S(t) = \iiint_V M_\perp(0) \exp(i\gamma \Delta H_z(x,y,z) \cdot t) dx dy dz \qquad (1)$$

where $\Delta H_z(x,y,z)$ represents the local induced field, i.e. the offset from the nominal field.

Based on a magnetic surface-charge model, Hwang and Wehrli [4], computed the induced magnetic field from 3D trabecular bone images and showed the local field to result in a distribution whose mean and variance depend on the orientation of the static magnetic field relative to the structure. These findings are, of course, a consequence of the structural anisotropy of trabecular bone, which is known to grow and remodel in response to the stresses to which is subjected (Wolff's Law). Since the induced magnetic surface charge density scales as the scalar product of the surface normal $\mathbf{n}$ and the applied magnetic field $\mathbf{H}_0$ as

$$\sigma \approx \mu_0 \Delta\chi \mathbf{H}_0 \cdot \hat{\mathbf{n}} \qquad (2)$$

(valid as long as for the susceptibility difference between the two materials, $|\Delta\chi| \ll 1$ holds), trabecular plates perpendicular to the applied field get magnetized preferentially. There are various approaches to compute the induced field. In [4] the authors resorted to a surface triangulation method by computing the induced field $\mathbf{H}_{induced}$ at location $\mathbf{r}$ as the sum of the induced fields from all source locations $\mathbf{r}'$ as

$$\mathbf{H}_{induced} = \sum_{p=1}^{N} \mathbf{H}_{induced,\,p}^{triangle} = \frac{1}{4\pi\mu_0} \sum_{p=1}^{N} \int_{T_p} \sigma(\mathbf{r}') \frac{(\mathbf{r}-\mathbf{r}')}{|\mathbf{r}-\mathbf{r}'|^3} dA' \qquad (3)$$

where N is the number of triangles and the integral represents the induced field from a single source location. The authors showed that the computation is greatly simplified by assuming that each triangular element has constant surface-charge density given by Eq. (2). The expected structural anisotropy is evident from the histograms of the induced magnetic field computed for the three orthogonal directions of the applied magnetic field relative to the major loading axis, shown for a specimen of human trabecular bone from the vertebrae (Fig. 1). The same authors subsequently evaluated their model by field mapping [5]. From the slopes of regression between the experimental and computed fields they obtained the absolute susceptibility of bone as -11.0×10^{-6} (S.I.), which is in close agreement with a reported value of -11.3×10^{-6} obtained with powdered bone by means of a spectroscopic susceptibility matching technique referred to previously [2].

The width of the induced magnetic field distribution over the sample volume (such as an imaging voxel) can be measured, for example with an asymmetric echo technique for which the echo amplitude evolves as $\exp(-2\tau/T_2')$ where τ is the echo offset [6].

Other pulse sequences based on combining RF and gradient echoes such as GESFIDE (gradient-echo sampling of FID and echo) [7] or GESSE (gradient-echo sampling of spin echo) [8] yield both T_2 and T_2^* and thus T_2' as $1/T_2^* - 1/T_2$. The full width at half maximum, ΔH, of the distribution of the induced field, $P(H_{induced})$, then is related to T_2' as $T_2' = \gamma\Delta H/2$. Spectroscopic approaches have also been practiced to obtain T_2^* from the line width of the marrow water or methylene resonance [9].

Yablonskiy and Haacke had previously developed a theory for magnetically heterogenous materials such as trabecular bone or networks of blood vessels, showing that the concept of an exponential time constant T_2' is valid in the static dephasing regime, but only for decay times longer than a critical time t_c [10]. The static dephasing regime essentially implies that dephasing from local inhomogeneous fields is much faster than phase-coherence loss of magnetic moments as they visit sites of different magnetic field during diffusion, a condition that is generally satisfied for fatty bone marrow but, as we shall see, not necessarily in the cellular boundary zone lining the trabecular trabecular bone surface [11]. Yablonskiy and Haacke's model also showed R_2' (=$1/T_2'$) to scale with the volume fraction of the perturber (i.e. bone in the present case) and further that it has and angular dependence for anisotropic structures. The latter arrangement, as previously pointed out, is typical of trabecular networks, which preferentially align along the bone's major loading axis. For an array of mutually perpendicular struts and columns such similar to the trabeculae found in the vertebrae or in the radius (cf. Fig. 1), the model predicts R_2' to obey the following relationship [10]:

$$R_2' \propto \Delta\chi H_0 \left\{ \varsigma_h + \left(\varsigma_v - \frac{1}{2}\varsigma_h \right) \sin^2 \vartheta \right\} \qquad (4)$$

where ς_h and ς_v represent the volume fractions of struts and columns and θ is the angle between the magnetic field and the columns. The predictions of Eq. (4) are in good semiquantitative agreement with experimental findings in model structures [12,13], specimens of trabecular bone [14] as well as measurements in vivo in humans [15].

Measurements of T_2^* or T_2' have allowed discrimination of patients with osteoporotic bone loss and structural degradation of the trabecular bone network at various anatomic sites including the distal radius, vertebrae and hip, all common fracture sites, as well as at surrogate locations such as the calcaneus (for recent reviews of the subject, see, for example [16]). In general, regional relaxation rates were found to parallel apparent density measured by dual-energy X-ray absorptiometry or quantitative computed tomography. Some of this work has shown T_2' or T_2^* to discriminate patients with from those without fractures as well or better than bone densitometry [9,17]. However, the translational aspects of these methods are of primary interest to the clinical imaging community and are thus somewhat outside the intended scope of this article.

3.2. Diffusion in background magnetic field gradients

There has been recent evidence that the notion of the static dephasing regime, generally assumed to apply to protons in the marrow spaces exposed to the internal magnetic field gradient (IMFG) at the bone–bone-marrow boundary, may not necessarily be valid [18,19]. If the primary interest is the evaluation of the IMFG this can be achieved with a simple field map, obtained, for example from 3D high-resolution trabecular bone images, such as those reported by Hwang and Wehrli [4], yielding both magnitude and direction of the IMFG as $\nabla H_z(x,y,z)$ where $H_z(x,y,z)$ is the local induced magnetic field. Of course, such an approach would require imaging at a resolution adequate to resolve
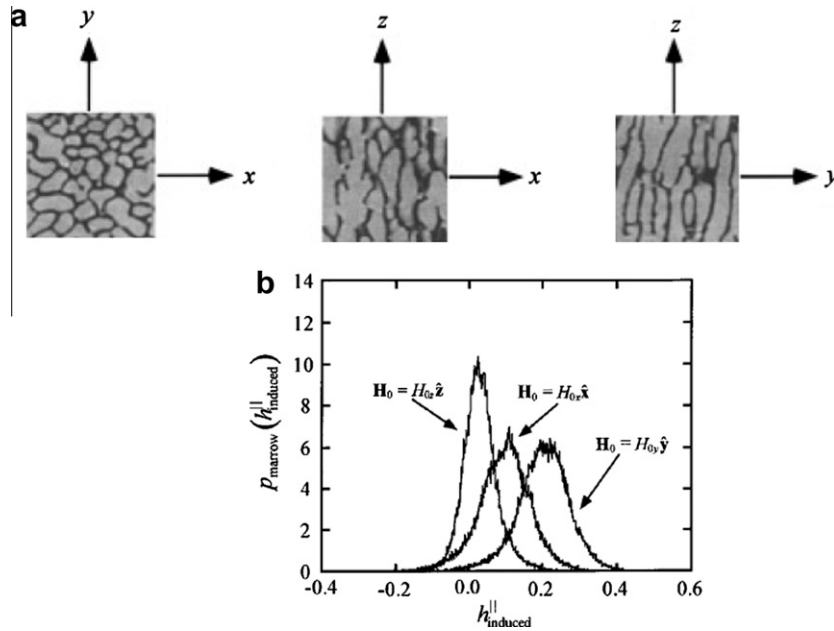
Fig. 1. (a) Orthogonal slices from a 3D image of trabecular bone from a human vertebral body. The superior–inferior axis is in the *z* direction. (b) P_{marrow} ($h_{induced}$) when H_0 is aligned with the *x*, *y*, or *z* axis (from [4], with permission).

individual trabeculae, which is not required for the methods quantifying T_2'. In fact, Yablonsky's theory requires operation in the *mesoscopic* scale where a statistical distribution of the perturber is present in the volume element, i.e. imaging voxel, therefore being applicable to the in vivo resolution regime.

Some of the more recent methods aimed at probing the IMFG in trabecular bone emerged from work in porous media, conceived by Song and colleagues at Schlumberger [20,21]. DDIF (decay of diffusion in internal gradients) is a method based on collecting a stimulated echo, which is modulated by diffusion in IMFGs caused in the pore spaces of heterogenous materials such as rocks. The basic idea is to sample the stimulated echo signal as a function of diffusion time. Laplace inversion of this signal after correction for decay caused by T_1 relaxation yields what has been referred to as a 'DDIF spectrum' from which the pore size distribution can be inferred [20]. The basic DDIF pulse sequence for which also imaging implementations were designed [18,19], is shown in Fig. 2. For large pores as in the case of trabecular bone, with pore volume fractions on the order of 80%, the IMFG is confined to a region encompassing tens of micrometers at most. As a result the DDIF parameters are sensitive to the surface-to-volume ratio [18].

For small sampling volumes, i.e. imaging voxels smaller than the typical structural length scale the DDIF rate, $1/T_{DDIF}$, is given by [18]

$$1/T_{DDIF} = 1/T_{back} + \gamma^2 G_{int}^2 t_e^2 D \qquad (5)$$

where $1/T_{back}$ is the background relaxation rate, essentially the longitudinal relaxation rate and contributions from diffusion attenuation due to the imaging gradients. Hence, the mean square internal gradient can be computed from Eq. (5). In contrast, for large sampling volumes, i.e. voxels more characteristic of the low-resolution imaging regime in which structural elements typically are not resolved, the DDIF signal exhibits multiexponential behavior commensurate with a distribution of G_{int}.

Fig. 3 shows DDIF data in specimens of trabecular bone from recent work by Sigmund et al. [18] highlighting the characteristically different decay behavior for samples differing in structural makeup. For example, there was a strong correlation between the short decay fraction and the projected surface area. Similar data were

subsequently obtained by the same group of authors from images obtained in various resolution regimes illustrating the potential of the method to characterize structural properties [19].

Common to the work described above is that it is based on specimen data and further that the experiments were performed after bone marrow removal and suspension in water. The key difficulty to overcome in translating the method to studies in vivo are the diffusion characteristics of bone marrow constituents. At many skeletal locations the marrow is predominantly of the yellow type (for example in the distal extremities), with the dominant signal-producing entity being fatty acid glycerides (FAT). Alternatively, such as in the vertebrae, marrow is mixed, i.e. consisting of both yellow and read marrow, with water being the major constituent in the latter. Since the diffusion coefficient of FAT is two to three orders lower than that of tissue water, diffusion attenuation is expected to be far lower for the former. However, very recent work in Silvia Capuani's laboratory shows that even at locations of predominantly fatty marrow, diffusion of the water in the cellular boundary layer adjoining the bone surface is sensitive to internal gradients (Fig. 4). Their approach to obtain a collective measure of the IMFG differs from the DDIF approach. Instead, de Santis
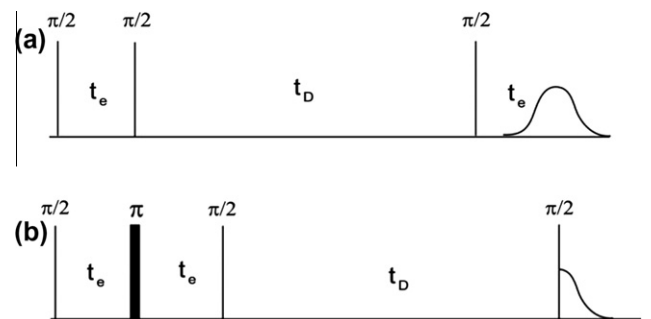

Fig. 2. (a) DDIF pulse sequence; (b) reference pulse sequence yielding T_1. Timing parameters t_e and t_D represent encoding and diffusion time periods, respectively. An echo signal is detected for DDIF, and an FID is detected for the reference sequence. For imaging the RF pulses are made spatially selective and an imaging module is added. (from Ref. [18] with permission).
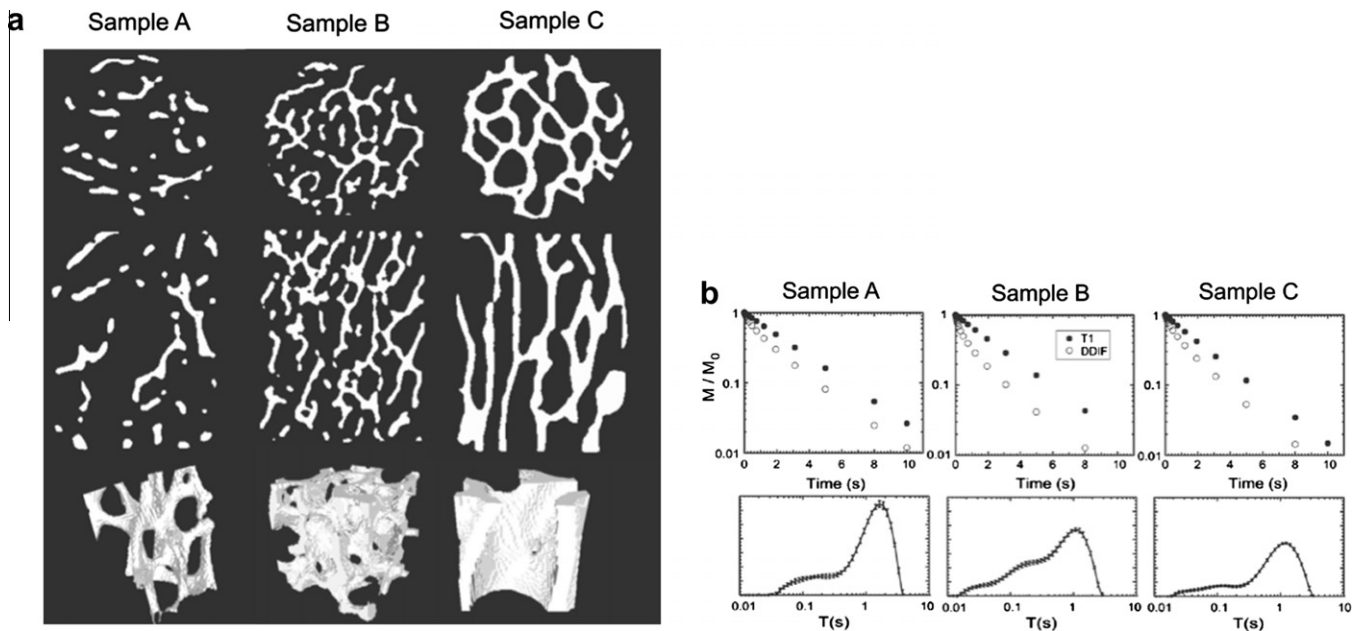
Fig. 3. (a) Micro-CT images of bovine tibia trabecular bone samples (top: longitudinal section center: transverse section; bottom: volume rendered image). After marrow removal samples were immersed in saline and subjected to the pulse sequences of Fig. 2. (b) DDIF signal versus diffusion time (top) and resulting DDIF spectra after Laplace inversion of T_1-corrected signal (bottom). Particularly notable is the higher spectral weight of the short-decay time region for the very dense sample B. (from [18], with permission).
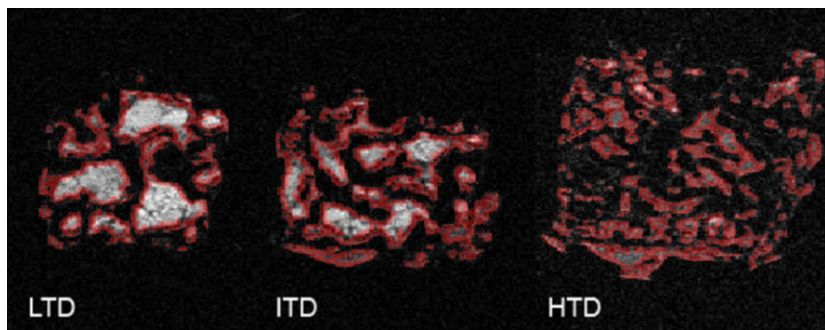

Fig. 4. Trabecular bone specimen MR images from which the data in Table 1 were obtained. Acronyms refer to low, intermediate and high trabecular density (LTD, ITD, HTD). Red mask superimposed on the images marks the water containing boundary zone in which water molecular diffusion is assumed to occur (from [11] with permission).

et al. [11] collected a train of CPMG echoes whose amplitude is attenuated due to both T_2 relaxation and diffusion:

$$S(TE) = S_0 \exp[(-TE/T_2^{true}) - (\gamma G_i)^2 \cdot ADC \cdot (TE)^3] \qquad (6)$$

where T_2^{true} is the true transverse relaxation rate, G_i is an average internal gradient, and ADC is the apparent diffusion coefficient. The authors then separately determined ADC and T_2^{true} and extracted G_i by curve fitting in experiments on intact calf tibia trabecular bone samples. In their interpretation the latter represents a dynamic average of the IMFG. Experiments were done both in bulk in spectroscopy mode and by fat suppressed imaging at 400 MHz. T_2, ADC, G_i for water and fat are listed in Table 1. Of interest is the inverse dependence of ADC and internal gradient on trabecular density, which is only present for the water component (Table 1a). ADC for the lipid component was found to be two orders of magnitude lower and independent of trabecular architecture, with the internal gradient determined by the fat–water interface. The authors have since extended their work to the study of patients with independently diagnosed osteoporosis or osteopenia and shown at 3 T field strength that the IMFG measured in the calcaneus

(the densely trabeculated heel bone) strongly differentiated patients with low bone density from their healthy peers.

4. Assessment of cortical bone composition and structure

4.1. Bone water and collagen

The structural and physiologic organization of cortical bone substantially differs from its trabecular counterpart. With a porosity on the order of 5–20% it is far denser than trabecular bone, which typically has a pore volume fraction of 80% or greater. As pointed out previously, cortical bone is permeated by a network of channels, called Haversian and Volkman's canals that make up the large majority of the pore volume. Knowledge of pore volume fraction is of interest in that it increases with age [22] and particularly so in osteoporosis [23], thereby causing a significant decline in the bone's mechanical properties [24]. Water is the dominant chemical constituent present in the bone's pore space. However, a significant, typically larger, fraction of cortical bone water is collagen bound. Both fractions possess short T_2 and are thus not

Table 1
T_2, ADC, and G_i in three trabecular bone specimens of variable density with native marrow for both water (a) and fat component (b). Notable is the steep decreases in water ADC with trabecular density and commensurate increase in G_i. In contrast lipid ADC is independent of trabecular density (data from [11]).

	Water (%)	$T_2 \pm$ SD (ms)	$ADC \pm$ SD ($\times 10^{-10}$ m^2 s^{-1})	$G_i \pm$ SD (mT m^{-1})	$T_2^{true} \pm$ SD (ms)
(a) Water component					
LTD	55	17.0 ± 3.0	19.0 ± 0.4	222 ± 131	17.9 ± 1.0
ITD	47	15.0 ± 2.3	7.0 ± 0.4	282 ± 134	15.2 ± 0.5
HTD	97	14.8 ± 0.4	1.6 ± 0.1	803 ± 181	16.0 ± 0.3
(b) Fat component					
	Fat (%)	$T_2 \pm$ SD (ms)	$ADC \pm$ SD ($\times 10^{-10}$ m^2 s^{-1})	$G_i \pm$ SD (mT m^{-1})	$T_2^{true} \pm$ SD (ms)
LTD	45	42.3 ± 6.2	5.3 ± 0.3	760 ± 195	43.0 ± 4.8
ITD	53	39.7 ± 4.0	5.9 ± 0.3	727 ± 437	44.0 ± 5.3
HTD	3	31.6 ± 6.0	5.4 ± 0.2	904 ± 119	37.5 ± 9.8

detectable with conventional spin-echo or gradient-echo methods. However, the emergence of what is now termed "ultra-short echo time (UTE)" MRI during the past decade has made detection [25] and quantification [26] of bone water possible. UTE MRI has generally proven useful to make heavily collagenated connective tissues such as articular cartilage, tendon, ligaments, and bone "visible" [27]. We shall return to this topic following a brief review of the basic properties of the protons in the bone matrix and the insight recent NMR work has provided.

4.2. Spectral and relaxation behavior of bone water and collagen

Bone water is exchangeable with time constants for exchange, observed for example, by immersion in D_2O, on the order of tens of minutes to hours. Fernandez et al. studied the exchange behavior of bone water from which they determined the apparent diffusion coefficient of water using bulk exchange experiments as well as image-based measurements via finite-difference modeling of the diffusion equation [28]. The authors found an apparent diffusion coefficient in rabbit tibia of $7.8 \pm 1.5 \times 10^{-7}$ cm^2/s at 40 °C (close to physiological temperature), which is over two orders of magnitude slower than that of free water. The data are of interest in that they shed some light on diffusive transport of small molecules from the bone vascular system to the osteocytes, suggesting this process to occur within minutes.

The detectability of bone water hinges largely on the FID's lifetime. Fernandez et al. measured a line width of the proton signal in rabbit cortical bone at 9.4 T of 1 kHz corresponding ($T_2^* \sim 300$ μs) [29]. UTE image based measurements by Reichert et al. at 1.5 T in the human tibia yielded values of 400–500 μs [30], similar to those reported later by Techawiboonwong et al. at 3 T field strength [26,31]. The loss of the majority of the proton signal upon immersion in D_2O clearly showed these protons not to pertain to collagen, the major organic constituent of bone. The initial rapid decay of the post-D_2O exchange signal suggested a collagen proton T_2 at 9.4 T on the order of 20–40 μs in rabbit bone [29]. More recently, Horch et al. [32] performed a detailed spectroscopic and relaxometric investigation of the proton NMR signal in human cortical bone of the femur at 4.7 T. T_2 relaxation spectra were obtained from the echo envelope of a CPMG train with 10,000 echoes were collected at 100 μs echo spacing by fitting the echo amplitudes to a weighted sum of exponentials. The authors found two submillisecond components with T_2 values of 57 ± 4 and 416 ± 35 μs, which they assigned to collagen and collagen-bound water, as well as long-lived components ranging from tens to several hundred milliseconds (Fig. 5a). Their assignment of the short components was further supported by 2D $T_2 - T_2$ relaxation exchange spectroscopy (REXY) [33] (Fig. 5b). From a quantitative analysis the authors concluded about 70% of total water to be collagen-bound. While these results agree at least semiquantitatively with those obtained with other methods [34], the illposedness of the problem, in

particular in the presence of noise and an a priori unknown number of relaxation components, remain a concern [35].

A further indication in support of the assignment of the T_2 relaxation-based assignment of the dominant fraction to collagen-bound water are the findings for T_1, which is far shorter than expected if the majority of the water were contained in the pores of the Haversian canal system. Actual values reported range from 140 to 260 ms [30] at 1.5 T in the human tibial cortex, increasing with age. At 3 T somewhat longer values were found at the same anatomic location, averaging 398 ± 7 ms in five donors, ages 57–79 years. The unusually efficient T_1 relaxation therefore is indicative of significant motional hindrance.

Ong et al. pursued another approach for unambiguous assignment and quantification of collagen-bound and pore water pools via deuterium NMR [34]. It is well known that collagen-bound deuterium oxide in heavily collagenated, motionally rigid, connective tissues such as tendons or articular cartilage, gives rise to quadrupole splittings (see, for example, [36], for a recent review of the subject). The magnitude, v_Q of the splitting is given by

$$v_Q = \sum_i v_i P_i (3\cos^2\theta_i - 1)/2 \qquad (7)$$

where v_i and P_i represent the splitting and population of the *i*th binding site, and θ_I is the angle between the director – typically the direction of the collagen fibers – and the magnetic field. Accordingly, the largest splitting is expected when the osteon is parallel to the B_0. Since osteons in cortical bone are oriented with their axes parallel to the major loading direction, this coincides with the macroscopic axis for bone from the shaft of the tibia or femur. A similar relationship is expected for protons, in which case the origin of the splitting is dipole–dipole coupling. However, the phenomenon is not commonly observed since proton dipolar split water signals are more sensitive to exchange averaging [37]. Further, as a significant fraction of the tissue water is not ordered (i.e. pore water), the splittings may be partially or fully masked by singlet resonances. One solution is to eliminate the undesired signals by double-quantum filtering. There are multiple approaches to this problem but a convenient pulse sequence (for which also imaging implementations have been reported [36]) is the IP-DQF sequence

$$90° - \tau - 90° - t_{DQ} - 90° - \tau - 90° - t_{ZQ} - 90° (Acq) \qquad (8)$$

which returns in-phase spectra [37]. Here τ is the creation time, t_{DQ} and t_{ZQ} are the double-quantum and zero-quantum evolution times. Setting of the creation time is critical for optimizing the signal amplitude for a particular magnitude of the splitting v_Q. The signal amplitude scales as $\sin(\pi v_Q \tau)$ indicating that the two signal components ought to be 180° out of phase with each prior to application of the second 90° pulse in [8] to yield maximum signal. Fig. 6a–c shows 400 MHz proton spectra of a small specimen of human cortical bone before and after complete D_2O exchange. Of particular relevance are the post-D_2O exchange DPF spectra showing a broad Pake doublet assigned to the methylene protons in collagen with a
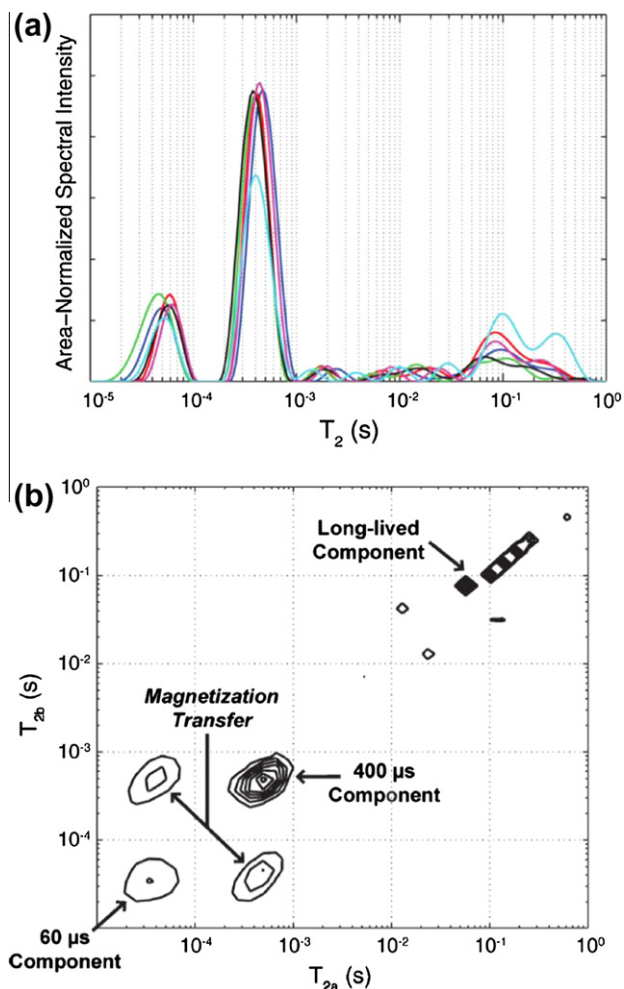
Fig. 5. (a) Proton T_2 spectra from six donors showing two sub-millisecond peaks and a broad envelope covering a band ranging from about 1 ms to 1 s. (b) Two-dimensional REXSY proton spectra showing cross-peaks between the two sub-millisecond signals, suggesting exchange between two pools during the 200-ms REXSY mixing period, indicative of spins exchanging via magnetization transfer mechanisms. Thus, the protons relaxing with $T_2 \sim 60$ μs and ~400 μs are in thermal contact during the mixing period while remaining isolated from the long-lived protons (from [32], with permission).

splitting of approximately 40 kHz, suggesting an order parameter between 0.5 and 1, consistent with the much higher rigidity of the collagen chains in calcified tissue. Of note is also the expected absence of angular dependence, a situation that is quite different for the deuterium quadrupole splittings of the water (Fig. 6d and e). Here, we find the quadrupole splitting to be approximately half of its value with the osteonal axis perpendicular as opposed to parallel to the field (4.3 versus 8.2 kHz), as predicted by Eq. (7).

While a direct comparison of the SQ and DQF spectra does not allow quantitative separation of the bound water from the total water pool, one can exploit the much longer T_1 of the pore water for separation by means of inversion nulling. In this manner Ong et al. [34] succeeded in quantifying pore water fraction achieving good agreement with micro-computed tomography (μCT) derived values. In 24 specimens from six donors varying in age from 27 to 83 years, pore volume fraction was found to increase from 2 to almost 40% correlating highly with μCT derived values with a slope close to unity and and near zero intercept. Conversely, bound water fraction correlated negatively with μCT porosity indicating an increase in pore volume fraction to occur at the expense of loss in osteoid and thus bound water. We shall see below that

image-based determination of these important structural parameters by proton UTE imaging may be feasible, even in vivo in human subjects.

4.3. Image-based visualization of sub-millisecond protons in calcified tissues

It was recognized early that the most common spatial encoding techniques based of phase encoding in the second dimension as in Cartesian sampling are generally not suited for imaging spins with very short transverse relaxation, such as quadrupolar nuclei or solids, as the delay imparted by the phase-encoding period entails signal losses. Radial acquisition techniques generally meet the requirement for minimizing the delay δ between the end of the RF pulse and beginning of sampling to satisfy $\delta \ll T_2^*$. The second requirement is for the RF pulse duration to be short enough so as to minimize coherence losses during the pulse ($\tau_{RF} < T_2^*$) [38]. Third, the sampling frequency bandwidth (BW) ought to be large enough so that for the total sampling time, $T_s \cong T_2^*$, as a means to minimize point-spread function (PSF) blurring.

The various methods being practiced for imaging short-T_2 biological materials only partially meet the above criteria, the key impediment in vivo often being specific absorption rate. Methods such as single-point mapping and their derivatives (e.g. SPRITE [39]) provide a relatively benign PSF but are inefficient otherwise. For imaging calcified connective tissues the family of radial 2D and 3D k-space mapping techniques sketched in Fig. 7 have emerged as favorites even though other methods, such as SWIFT [40], reviewed elsewhere in this special issue of the journal, should have merit too for the target applications discussed below.

Pulse design, pulse sequences and reconstruction for UTE MRI have recently been reviewed [41], as have methods and applications specific to bone [42]. Therefore, this section will be relatively brief, keeping the focus on quantification and translation from the laboratory to studies in patients. 2D UTE, a radial encoding technique based on half-pulses not requiring slice gradient rephrasing, was first described by Bergin et al. in 1991 [43] but remained little used until "rediscovered" by Robson et al. in 2003 [25]. This group of researchers recognized its potential for visualizing sub-millisecond T_2 tissues, in particular in conjunction with soft-tissue suppression techniques such as echo subtraction or inversion nulling. Since then the field has rapidly evolved both in terms of methodology and applications to the musculoskeletal (see, for instance [27]) and even the neurologic system [44,45].

Fig. 7 displays generic 2D and 3D pulse sequence diagrams for some of the sequences in current use for imaging short-T_2 tissues. Fig. 7a shows the sequence introduced by Robson et al. [25] involving half pulses with RAMP sampling. Notable is the requirement for two acquisitions of each radial line with opposite polarity of the slice-selection gradients. In this manner, the imaginary signal components cancel upon summing of the two signals [46]. Fig. 7b shows a hybrid 3D implementation differing from the former by inclusion of Cartesian sampling in the third dimension [47]. As a means to minimize echo time at $k_z = 0$ the slice-encoding gradient is stepped in time rather than in amplitude. Lastly, Fig. 7c and d display 3D radial sequences based on non-selective RF pulses with ramp sampling analogous to Fig. 7a (3D UTE) or with RF excitation in the presence of the encoding gradient (also referred to as 3D ZTE [48,49]). Since the latter fails to capture the lowest spatial-frequency signals, alternative means are required to collect the missing samples, such as resampling that portion of k-space at much lower gradient amplitude [50] or by single-point mapping as in PETRA (pointwise encoding time reduction with radial acquisition) [51]. A third option is algebraic reconstruction based on acquisition of pairs of radial projections with opposite polarity [48,52]. Fig. 8 illustrates the potential of ZTE for imaging teeth, the most densely
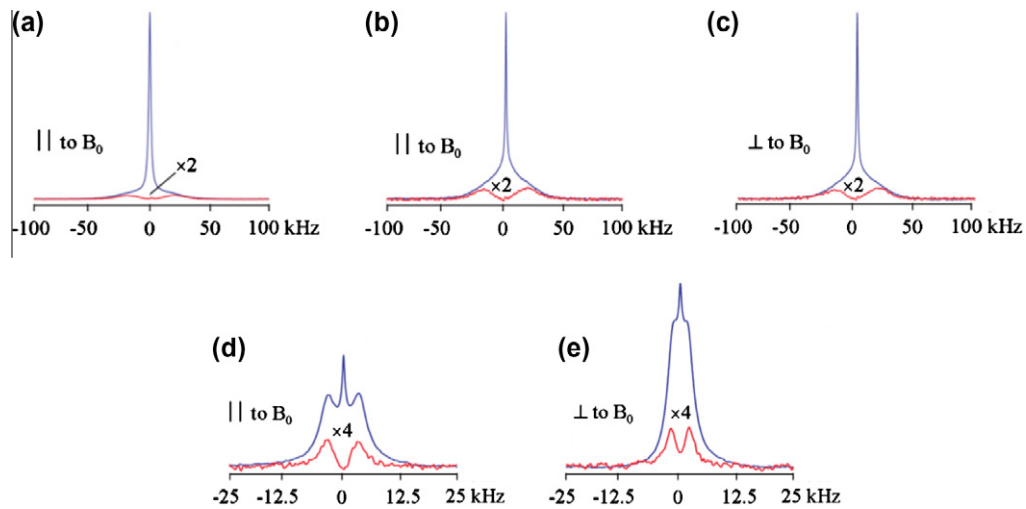
Fig. 6. 9.4 T proton and deuterium NMR spectra from a lamb tibia cortical bone specimen at 20 °C: (a) ^1H pulse-acquire and IP-DQF (at creation time, $t = 25$ μs) spectra before ^2H_2O immersion; (b and c) same as (a) after ^2H_2O immersion with bone parallel (||) and perpendicular () to the applied field, B_0. Note increased vertical scale relative to panel a to highlight the dipolar splitting. (d and f) ^2H pulse-acquire and IP-DQF ($t = 200$ μs) spectra after ^2H_2O immersion with bone || and to B_0 (from [34], modified).
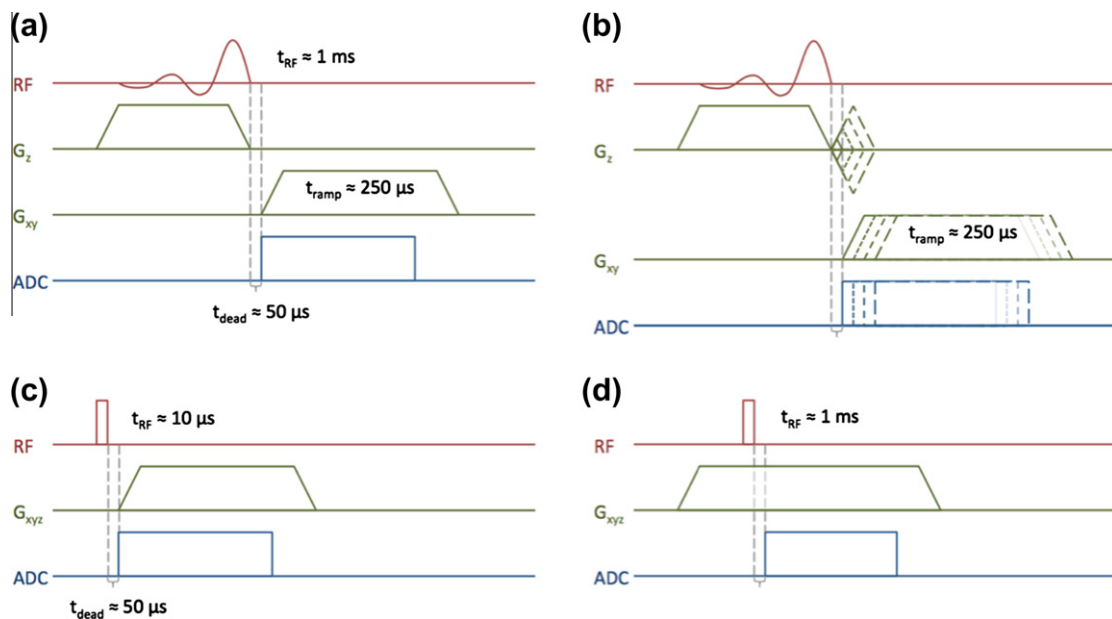

Fig. 7. Most common radial imaging techniques practiced in the author's laboratory for imaging short-T_2 calcified tissues on 1.5, 3 T and 7 T whole-body scanners: (a) 2D UTE with ramp sampling and slice-selective half-pulses; (b) 3D hybrid-UTE method with variable-TE slice-encoding to encode in the third dimension; (c) 3D UTE with ramp sampling following a non-selective excitation pulse; (d) 3D ZTE pulse sequence differing from (c) by the RF pulse being played out in the presence of the radial encoding gradient.

calcified tissue in mammals, suggesting that the method may be sensitive to subtle demineralization defects in carious teeth not detectable by X-ray imaging [48]. While these studies were conducted on extracted teeth ex vivo at 500 MHz, another recent paper highlights the possible applications of UTE MRI for examining teeth in situ in patients [53].

4.4. Suppression of soft-tissue signals

Detection of calcified tissues, most typically cortical and trabecular bone, calcified cartilage, teeth or extra-osseous calcifications, studied with the techniques outlined above, is hampered by the signals of the surrounding soft tissues. Not only are the latter's spin

densities far greater, their transverse relaxation times are at least two orders of magnitude longer. The need to selectively suppress the undesired signals has been recognized early and a variety of strategies have been offered. Most exploit the differential life times of the two proton species. In the simplest approach a second echo collected at TE $\gg T_{2,short}$ is subtracted from the UTE signal [30] but this method may be sensitive to gradient-induced eddy currents and, of course, sacrifices SNR as all subtraction methods do.

In 1992, Pauly et al. first proposed the use of saturation pulses that are long relative to T_2 of the fast-decaying spins of interest ($\tau_{RF} > T_{2short}$) showing that under these conditions only the long-T_2 soft-tissue protons are mutated, leaving the short-T_2 protons largely unaffected [46]. The design criteria and theory were

subsequently detailed by Sussman et al. [38] and various embodiments of the method are now in widespread use, including water and fat saturation consisting of successively applied frequency-selective saturation pulses (WASPI [50]) or dual-band saturation pulses [54]. Single and double-inversion nulling have also been practiced. In order to simultaneously suppress soft tissue signals arising from fat and water Du et al. applied adiabatic inversion pulses in succession, first on resonance with water and subsequently with the methylene proton chemical shift of triacyl glyceride (fat) in such a manner as to time the pulses so that the longitudinal magnetization of both components is nulled immediately prior to playing out the excitation half-pulse [55]. In contrast, the short-T_2 protons of the bone water are only saturated by the inversion pulses. Both inversion and saturation soft-tissue suppression methods can be combined with echo subtraction for additional efficiency of long-T_2 signal attenuation, albeit at the expense of an additional factor of $\sqrt{2}$ reduction in SNR. In a recent comparison of the various suppression techniques Li et al. concluded that combination of dual-band saturation UTE with echo subtraction to provide good short-T_2 SNR and CNR, albeit at the expense of greater sensitivity to B1 homogeneity. In distinction, IR-UTE was found to yield lower short-T_2 SNR efficiency while providing highly uniform short-T2 contrast [54]. Fig. 9 illustrates the spatial and T_2 selectivity of an adiabatic inversion preparation with a pulse bandwidth covering both water and fat spectra.

4.5. Quantification of water in calcified tissues

While mere visualization of protons that ordinarily elude detection by spin-echo based conventional imaging strategies is important in its own right as illustrated in the previous section, quantification of the water residing in the pore spaces of bone tissue versus that bound to the organic matrix, can provide new insight into the structural and molecular organization of the tissue [26,31,47,56,57]. Techawiboonwong et al. conceived a method based on calibration of the signal with a reference sample of known proton concentration and similar T_2 relaxation characteristics in specimens of human cortical bone from the tibia and subsequently in patients [26,31]. The transverse magnetization at time $t = TE$ can be written as

$$M_{xy}(TE) = C\rho_0 f_{xy} \frac{1 - e^{-TR/T1}}{1 - f_z e^{-TR/T1}} e^{-TR/T_2^*} \tag{9}$$

where f_{xy} and f_z represent the transverse and longitudinal magnetizations at the end of the RF pulse [38]:

$$f_{xy} = i \exp(-\tau/2T_2^* \gamma B_1 \tau \cdot \sin c \left[\sqrt{(\gamma B_1 \tau)^2 - (\tau/2T_2^*)^2} \right] \tag{10}$$

and

$$f_z = \exp\left(-\tau/2T_2^*\right) \cos\left[\sqrt{(\gamma B_1 \tau)^2 - (\tau/2T_2^*)^2} \right] + \tau/2T_2^*$$
$$\times \sin c \left[\sqrt{(\gamma B_1 \tau)^2 - (\tau/2T_2^*)^2} \right], \tag{11}$$

We see that under conditions where $\gamma B_1 \gg 1/2T_2^*$ the expressions for f_{xy} and f_z revert to the usual cosine and sine terms of the flip angle $\gamma B_1 \tau$. In a second regime, referred to as "critically damped" [38], the two terms balance each other ($\gamma B_1 \approx /2T_2^*$) and some transverse magnetization that is independent of the nominal flip angle is still generated:

$$f_{xy} = i \exp(-\tau/2T_2^*)\tau/2T_2^* \tag{10a}$$

while for the longitudinal mapping function the following is obtained:

$$f_z = \exp\left(-\tau/2T_2^*\right)\left(1 + \tau/2T_2^*\right) \tag{11a}$$

In the third regime, termed "overdamped", where $\gamma B_1 \ll 1/2T_2^*$ no excursion of the magnetization from the z-axis occurs, i.e.

$$f_{xy} \approx 0 \tag{10b}$$

and f_z becomes [38]:

$$f_z = \exp\left(-(\gamma B_1 \tau)^2/(\tau/T_2^*)\right) \tag{10b}$$

Eqs. (10) and (11) are valid for rectangular pulses but the two quantities need be computed numerically for selective pulses such as half-sinc pulses used in 2D UTE. In this situation, the actual transverse and longitudinal magnetizations deviate more significantly from their nominal values as the pulse duration is an order of magnitude longer than for non-selective pulses.

The authors in [31] validated their method in specimens of human cortical bone by means of deuterium exchange techniques whereby they measured the native water expelled from the bone after prolonged immersion in D$_2$O in comparison to measurements by UTE. They found the two methods to correlate ($r^2 = 0.99$, $p < 0.001$) but found that even after complete exchange there was a residual signal on the order of about 10%, which was attributed to non-exchangeable protons, likely pertaining to lipids. Further, a pilot study in a small group of pre- and postmenopausal women and patients with renal dystrophy showed bone water
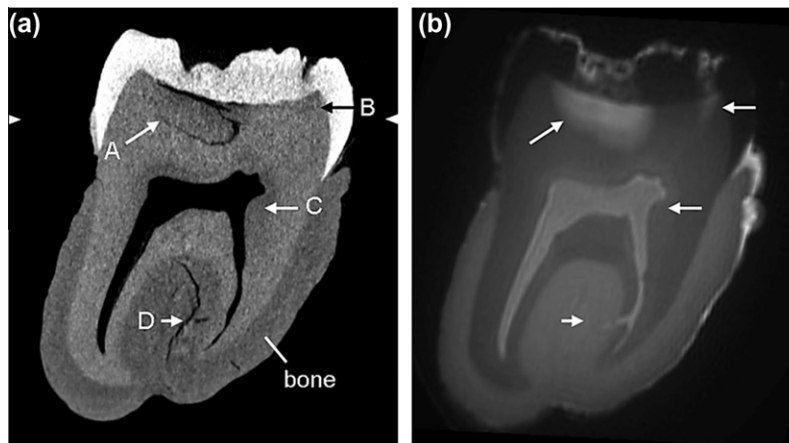

Fig. 8. Micro-CT (a) and proton ZTE image of extracted molar tooth obtained at 500 MHz in 6 min 55 s (b). The ZTE image displays large demineralized lesion (arrow A) with invasion into enamel, as well as a smaller lesion barely perceptible in the CT image (arrow B) appearing hyperintense in the MR image (from [48], with permission).
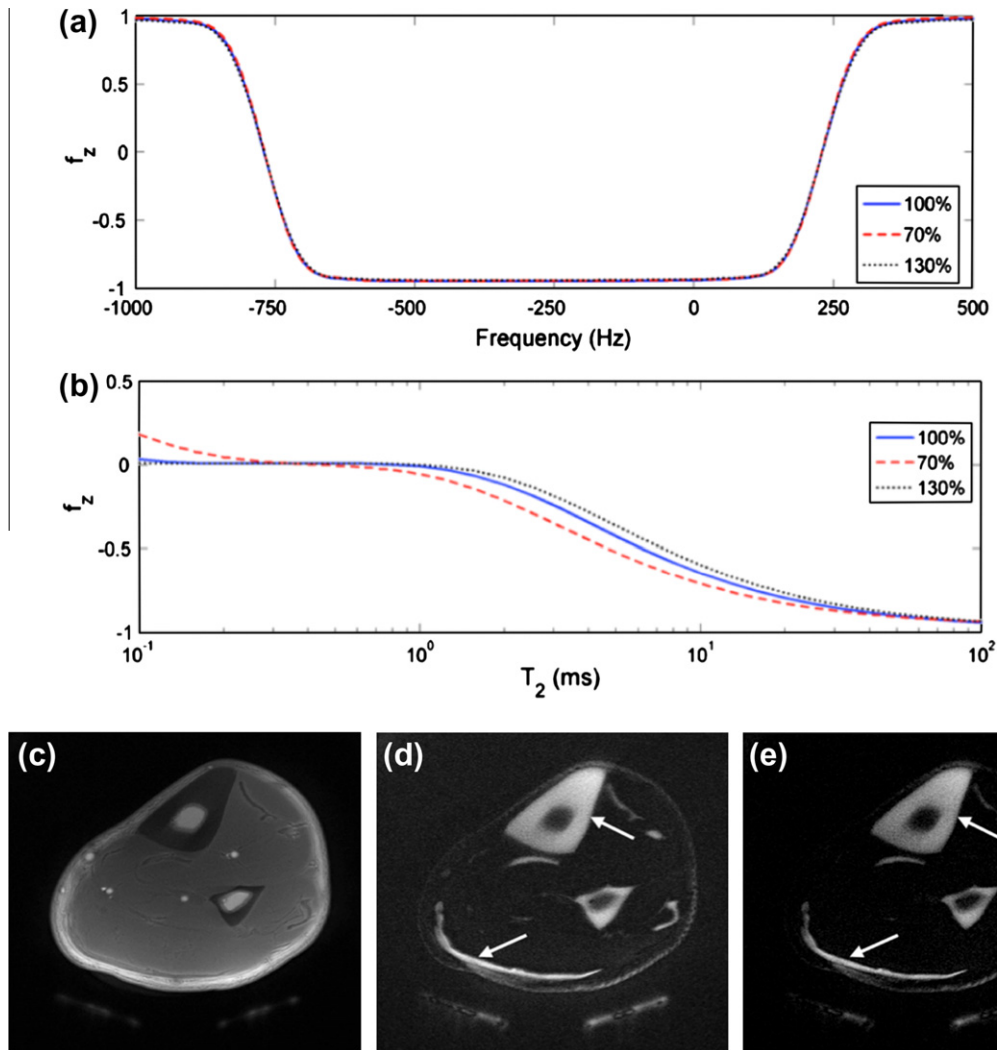
Fig. 9. Spatial and T_2 relaxation selectivity of adiabatic inversion: (a) inversion profile of 1 kHz-bandwidth hyperbolic secant inversion pulse for T_1 = 1 s, T_2 = 100 ms; (b) longitudinal magnetization as a function of T_2 indicating that protons with $T_2 \leqslant 1$ ms are saturated by the pulse. Also noted is the relative insensitivity of the effect of the pulse to deviations from desired B1 field (dashed and dotted lines). (c) unsuppressed first echo image (TE = 60 μs) at the mid-tibia obtained with a 2D UTE pulse sequence; (d) same with adiabatic inversion preparation; (e) difference image obtained by subtraction of second echo with TE = 4.6 ms. Arrows indicate tibia and Achilles tendon (modified, from Li et al. [54]).

measured by UTE MRI in the mid-tibia cortex to be greater by 65% (28.7 ± 1.3 versus $17.4 \pm 2.2\%$, $p < 0.001$) in the premenopausal than in the postmenopausal group, with the highest bone water concentration ($41.4 \pm 9.6\%$) found in the subjects with renal disease. The authors interpreted their findings as reflecting increasing porosity with age and particularly in subjects with end-stage renal disease. We have seen previously, however, that bulk measurements based on T_2 relaxometry [32] and deuterium NMR [34] support the notion that a greater fraction of bone water is collagen bound as opposed to pore-resident. Thus, increased pore water fraction can only occur as a result of a decrease in osteoid volume and thus a decrease in collagen-bound water, thereby suggesting two opposing, potentially mutually canceling effects. However, because of the greater volume density of pore water, a reduction in a given amount of bone tissue will result in a disproportionate gain in pore water. It is for this reason that bulk water fraction was also found to correlate with independently measured pore volume fraction, as observed by Ong et al. [34]. Nevertheless, noninvasive separation of the two water fractions would be desirable as a means to evaluate porosity indirectly, i.e. without the need to resolve individual pores.

Diaz et al. [58] hypothesized that pore water, by virtue of its greater mobility, should have longer T_2^*. The authors then showed in bovine cortical that the T_2^* decay fit a bicomponent model

$$S(T_2^*) = A_S \exp\left(-\frac{t}{T_{2s}^*}\right) + A_l \exp\left(-\frac{t}{T_{2l}^*}\right) \tag{12}$$

with A_s and A_l being the fractions of the short and long T_2^* components, which they found to be on the order of 80% and 20% and 300 μs and 2 ms, respectively, and which they attributed to bound and free water. In subsequent work from the same group, Bae et al. [59] found the two water populations to be correlated with μCT-derived porosity; positively with the free water fraction and negatively with the bound water fraction (both $R^2 = 0.25$, $p < 0.001$), in good qualitative agreement with the work by Ong et al. [34], discussed above. Therefore, the results lend credence to the authors' assignments suggesting the long-T_2^* component to be predominantly composed of free, i.e. pore water, and thus pore volume fraction. Horch et al. questioned the validity of the T_2^* relaxometric approach arguing that the pore water NMR line should be inhomogeneously broadened by virtue of the expected large range
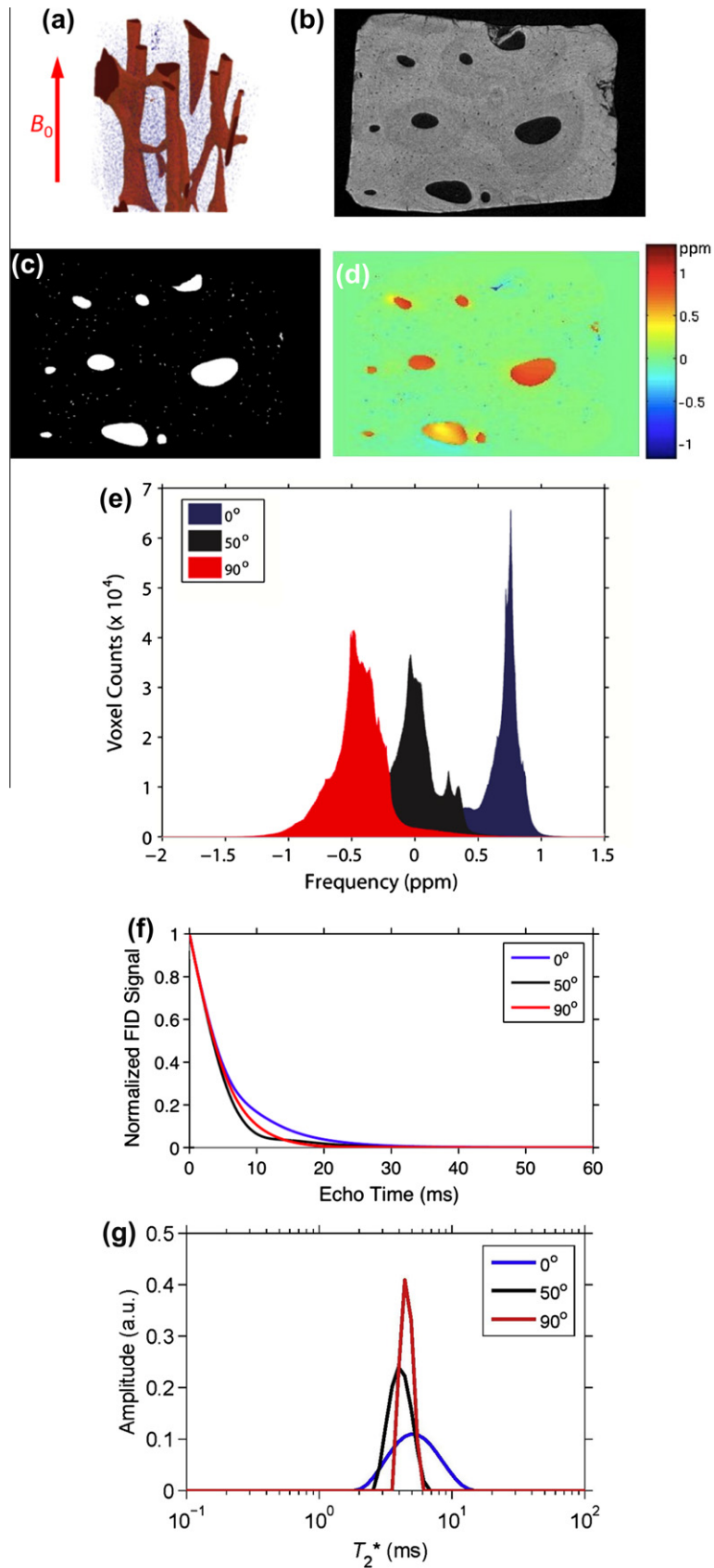
Fig. 10. Induced magnetic field in the pore space of the Haversian system: (a) 3D rendition of a small volume of human cortical bone of the mid-tibia obtained at 1 μm isotropic voxel size; (b) cross-sectional image; (c) segmented image (pore space white); (d) induced magnetic field in the pore spaces computed from Eq. (13) assuming a volume susceptibility $\Delta\chi = 4\pi \cdot 0.19$, showing section across 3D volume; (e) histogram of induced field for three orientations of the osteonal axis relative to B_0; (f) predicted decay of the UTE signal computed from Eq. (14) for three orientations relative to the magnetic field; (g) T_2^* spectra obtained by inversion of the FIDs in (e) (C. Li et al., unpublished).

of resonance frequencies governed by pore-matrix susceptibility and pore geometry [60].

We tested this hypothesis by computing the induced field similar to the approach in [4] for trabecular bone except that much higher-resolution images are required since the pore sizes in cortical bone are one to two orders of magnitude smaller than those of the spaces between adjacent trabeculae. The induced magnetic field ΔB in the pore spaces of the Haversian and lacunar system of cortical bone was computed by means of the fast Fourier approach in k-space (see, for example [61]) as

$$\Delta B(x,y,z)/B_0 = FT^{-1}\left(FT(\Delta\chi(\mathbf{r}))\left(\frac{1}{3} - \frac{(k_z cos\theta - k_y sin\theta)^2}{k_x^2 + k_y^2 + k_z^2}\right)\right) \quad (13)$$

where FT is the Fourier operator, $(\Delta\chi(r))$ is the spatial distribution of the relative magnetic susceptibility at spatial location $\mathbf{r}(x,y,z)$ (obtained from the 3D image after segmentation into bone and pore space). The expression $\left(\frac{1}{3} - \frac{(k_z cos\theta - k_y sin\theta)^2}{k_x^2 + k_y^2 + k_z^2}\right)$ is the Fourier transform of the convolution kernel representing the dipole field $d = \frac{1}{4\pi}\frac{3cos^2\theta - 1}{|r|^3}$ and θ is the angle of the x-axis relative to the applied field B_0. Fig. 10a–d show a 3D rendition of a small volume of cortical bone, along with a map of the induced field. In Fig. 10e, the histogram of the induced field is displayed for three orientations of the specimen axis relative to the magnetic field showing characteristic shifts similar to those predicted previously in trabecular bone [4] and observed experimentally in specimens [14] and humans in vivo [15]. The predicted FID and T_2^* relaxation spectrum is shown in Fig. 10f and g. In order to simulate T_2 (as a means toward predicting T_2^* as the sum $1/T_2 + 1/T_2^*$) a surface relaxation model was used similar to the one described by Wang et al. to estimate CPMG decays rates in cortical bone [62]. It is based on the concept that $1/T_2 = \rho \cdot S/V$ where ρ is the surface relaxivity, S is the pore surface and V its volume. Since surface relaxivity is unknown pore water T_2 was assumed to cover a range of 10 ms and the signal $s(t)$ was calculated as the sum of contributions from each pore voxel i as

$$s(t) = \sum_i \exp(-t/T_{2,i} + j2\pi\gamma B_i t). \quad (14)$$

where ΔB_i is the induced field in pore voxel i and summation is over all pore voxels. The two terms in the equation thus represent damping from surface relaxation and static dephasing. Since the voxel is much smaller than the pore size (1 μm versus ⩾20 μm) it is reasonable to consider the field to be approximately constant across the voxel. We note the preliminary nature of these data requiring corroboration in other specimens as well as experimental verification. Nevertheless, the predicted T_2^* is of the order observed in cortical bone specimens and in vivo by bi-component analysis [59].

4.6. Bone mineral

Mineral density is commonly assessed by X-ray based modalities, either dual-energy X-ray absorptiometry or quantitative computed tomography, which provide a density measure expressed in g/cm^2 or g/cm^3, respectively. Both methods use ionizing radiation even though the former's dose is minimal. The density measurements are non-specific and are apparent in the sense that the resolution is such that reduced tissue mineralization could not be distinguished from bone of greater microporosity. This ambiguity, it has been argued [63], precludes distinction of osteoporosis in which bone becomes porous but is generally normally mineralized, from osteomalacia, a disorder in which the bone is hypomineralized. The same group of authors reasoned that true mineralization density (variably also denoted 'degree of mineralization of bone', DMB [64] or 'extent of bone mineralization' [65]) could be obtained

by quantifying matrix volume (i.e. the fractional volume of bone occupied by bone tissue). Cao et al. [65] achieved this goal by solid-state radial imaging with water and fat suppression (WASPI [50]) in conjunction with a polymer blend of matching relaxation times serving as a calibration standard. Hence, phosphorus density via solid-state ^{31}P imaging, whose feasibility was first shown by Wu et al. [66] and matrix volume, would allow derivation of DMB.

While path delineated above toward noninvasive quantification of DMB is plausible, the method is fraught with difficulties. Chief among these are the extremely unfavorable relaxation properties of ^{31}P in bone mineral with T_2/T_1 ratios on the order of 10^{-5}–10^{-6} depending on field strength [67] (compared to about 0.02 for protons in soft tissue). Nevertheless, 3D radial ^{31}P imaging in animal models has yielded unique information on mineralization in model systems of osteomalacia [68] and response to antiresorptive treatment [69]. The very short T_2 of ^{31}P in bone mineral and its further shortening with field strength (reaching 120 μs at 7 T) is likely a consequence of the significant chemical shift anisotropy of hydroxyl apatite ($\sim$40 ppm) [70]. Besides adversely affecting SNR, point-spread function blurring limits the effective resolution to a few millimeters. In spite of these adversities Wu et al. [71] recently have been able to acquire ^{31}P images of the human wrist in vivo at 3 T field strength on a clinical scanner with a custom-built birdcage transmit-receive coil (Fig. 11). The critical hurdle to overcome was to shorten the receiver dead-time in the spectrometer's ^{31}P RF chain, which the authors accomplished by mixing the proton transmit pulse frequency with the frequency from an external synthesizer. In this manner they achieved an effective delay from the end of the pulse to the start of data acquisition of 20 μs.

5. Direct detection of trabecular architecture via high-resolution marrow MRI

Much work has been focused on methods for direct visualization and quantification of structure at length scales resolving individual trabeculae. However, in spite of advances in pulse sequence methodology and RF coil design, in vivo structural imaging of trabecular bone architecture largely remains confined to peripheral skeletal locations such as the wrist and ankle. Here, closely coupled receive coils ensure that adequate SNR levels can be attained, currently allowing for voxel volumes as small as 4×10^{-3} mm^3 at 3 T field strength [72]. Notably, these are one to two orders of
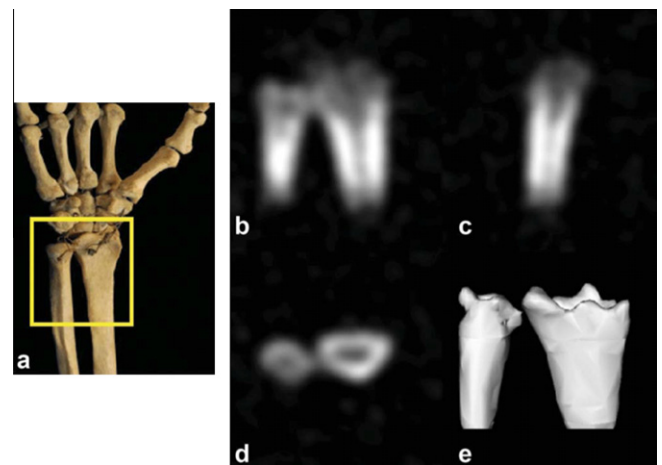

Fig. 11. In vivo ^{31}P 3D radial MRI of bone mineral of the wrist of a healthy 41-year-old male volunteer. (a) Schematic view of the scanned region. (b–d) Posterior–anterior, lateral and transverse image slices; (e) three-dimensional iso-surface rendering of the full dataset. Distal radius and ulna including marrow cavity are clearly visualized (from [71], with permission).

magnitude lower than those practiced in structural imaging of the musculoskeletal system. Since much of the technology and applications have been reviewed in recent years (see, for instance, [16,73] and references cited) only the most recent pertinent developments will be discussed. Lastly, it needs to be pointed out that MRI competes with CT as both modalities have demonstrated their ability to yield structural information (see, for instance [74]).

Initially, structure evaluated in terms of scale, topology and orientation of the trabecular networks had been given the most attention as possible surrogates for bone strength and for assessing fracture susceptibility in patients [75]. For example, it is known that bone loss occurring during aging, and at an accelerated pace in osteoporosis, entails perforation of trabecular plates, leading to conversion of plates to rods [76], thereby disproportionately weakening the structure [77]. Since trabeculae orient along the major stress lines, various measures of structural orientation, including mean intercept length [78] and spatial autocorrelation analysis [79] have been applied as a means to mathematically describe structural anisotropy from in vivo MR images [80]. Wald et al., on the basis of in vivo images of the distal tibia, were able to show that bone volume fraction and indices of structural anisotropy predicted the bone's mechanical competence with high accuracy [81].

More recently, there has been a shift toward exploiting the capabilities of obtaining images representative of partially or fully resolved 3D structural images as input into finite-element (FE)

solvers, typically after converting voxels to hexahedral finite elements [82]. Since in spin-echo imaging marrow protons are the signal producing entities while pure bone appears with background intensity (as bone water cannot be detected at typical echo times on the order of several milliseconds), the raw images are processed to yield parametric images in which signal amplitudes represent the fractional voxel occupancy by bone (i.e. bone volume fraction maps) [83]. Full validation of the structural indices would require mechanical testing on specimen images obtained at comparable resolution. However, there is compelling evidence from earlier work based on high-resolution micro-computed tomography that indicates good agreement between FE derived indices and mechanical test results [84] and further, that the predicted mechanical indices obtained in a resolution regime of in vivo imaging are strongly correlated with those derived by high-resolution CT imagery [85].

MR image based FE analysis has shown potential as a means to assess the response to intervention in patients with various disorders of bone mineral homeostasis such as treatment with drugs preventing bone resorption or enhancing bone formation [87,88] or to evaluate the implications of organ transplantation [86]. In [86], the authors showed that 6 months following renal transplantation both cortical and trabecular bone stiffness estimated in the distal tibia decreased, presumably as a result of exposure to large doses of steroids. Fig. 12a–c shows a single image from a 3D image
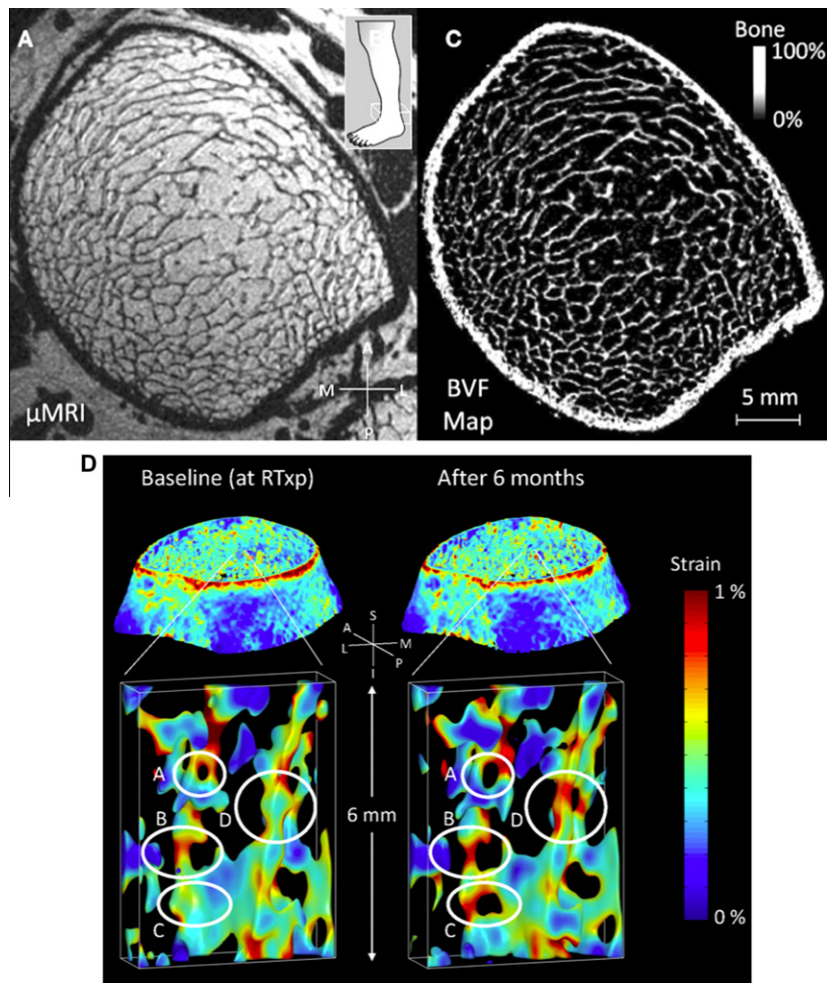

Fig. 12. (a) Axial view of MR image obtained at the left distal tibia (b, inset) from a 25-year old woman at $137 \times 137 \times 410\ \mu m^3$ voxel size. (c) Bone-volume-fraction (BVF) map derived from A representing the fractional occupancy of bone linearly scaled between 0% (pure marrow) and 100% (pure bone) at each voxel. (d) Comparison of strain maps obtained from whole-bone at time of kidney transplantation and 6 months thereafter. Magnified 1 mm $\times$ 2 mm $\times$ 6 mm regions highlight alterations occurred in the trabecular bone network between the two time points: (A) enlargement of a perforation, (B) thinning of a vertical trabecula, (C) a plate-to-rod conversion, and (D) strain accumulation due to bone loss (from [86], with permission).

array along with processed bone volume fraction map for FE modeling. Magnified strain energy maps at two time points highlighting local structural and mechanical alterations are displayed in Fig. 12d.

FE modeling in the nonlinear regime to predict the bone's yield and post-yield behavior has also come of age, thanks to algorithmic advances and the unprecedented computing power that has become available with multi-core desktop computers and the ever-decreasing cost of RAM [83]. Recent work in the author's laboratory shows that fracture toughness (energy required for the bone to fail) obtained as $\int \sigma(\varepsilon)d\varepsilon$ where σ and ε represent stress and strain, and integration is to peak strain, is not well predicted by linear indices such as stiffness [89].

MRI based FE methodology is still in its infancy and, except for the wrist, the major fracture sites are the femur and vertebrae, anatomic locations at which high-resolution imaging is more difficult. Much of this work has been performed for compressive loading, which is rarely the failure mechanism that leads to fracture. Further, MRI currently provides only limited information on the intrinsic material properties determined by mineral density and composition, or chemical modification occurring in collagen (e.g. nature and extent of cross-linking, water binding, etc.), some of which have been discussed previously. Lastly, the material modulus is generally assumed to be isotropic even though this is known not to be correct given the highly anisotropic nanostructure of this complex biomaterial.

In summary, some of the work discussed in this article, shows that NMR and MRI can provide unprecedented insight into structure and function of calcified tissues nondestructively, and in many instances, noninvasively, in animals and humans. Further advances are difficult to anticipate just as much of what we now take for granted was entirely unforeseeable a mere two decades ago.

References

[1] R. Ritchie, M. Buehler, P. Hansma, Plasticity and toughness of bone, Phys. Today (2009) 41–47.
[2] J.A. Hopkins, F.W. Wehrli, Magnetic susceptibility measurement of insoluble solids by NMR: magnetic susceptibility of bone, Magn. Reson. Med. 37 (1997) 494–500.
[3] F.W. Wehrli, J.C. Ford, M. Attie, H.Y. Kressel, F.S. Kaplan, Trabecular structure: preliminary application of MR interferometry, Radiology 179 (1991) 615–621.
[4] S. Hwang, F. Wehrli, The calculation of the susceptibility-induced magnetic field from 3D NMR images with applications to trabecular bone, J. Magn. Reson., Ser. B 109 (1995) 126–145.
[5] S.N. Hwang, F.W. Wehrli, Experimental evaluation of a surface charge method for computing the induced magnetic field in trabecular bone, J. Magn. Reson. 139 (1999) 35–45.
[6] K. Engelke, S. Majumdar, H. Genant, Phantom studies simulating the impact of trabecular structure on marrow relaxation time, T_2' phantom studies, Magn. Reson. Med. 31 (1994) 380–387.
[7] J. Ma, F.W. Wehrli, Method for image-based measurement of the reversible and irreversible contribution to the transverse relaxation rate, J. Magn. Reson., Ser. B 111 (1996) 61–69.
[8] D.A. Yablonskiy, E.M. Haacke, An MRI method for measuring T2 in the presence of static and RF magnetic field inhomogeneities, Magn. Reson. Med. 37 (1997) 872–876.
[9] F. Wehrli, L. Hilaire, M. Fernández-Seara, B. Gomberg, H. Song, B. Zemel, L. Loh, P. Snyder, Quantitative magnetic resonance imaging in the calcaneus and femur of women with varying degrees of osteopenia and vertebral deformity status, J. Bone Miner. Res. 17 (2002) 2265–2273.
[10] D.A. Yablonskiy, E.M. Haacke, Theory of NMR signal behavior in magnetically inhomogeneous tissues: the static dephasing regime, Magn. Reson. Med. 32 (1994) 749–763.
[11] S. De Santis, M. Rebuzzi, G. Di Pietro, F. Fasano, B. Maraviglia, S. Capuani, In vitro and in vivo MR evaluation of internal gradient to assess trabecular bone density, Phys. Med. Biol. 55 (2010) 5767–5785.
[12] K. Selby, S. Majumdar, D.C. Newitt, H.K. Genant, Investigation of MR decay rates in microphantom models of trabecular bone, J. Magn. Reson. Imaging 6 (1996) 549–559.
[13] D.A. Yablonskiy, Quantitation of intrinsic magnetic susceptibility-related effects in a tissue matrix. Phantom study, Magn. Reson. Med. 39 (1998) 417–428.
[14] H. Chung, F.W. Wehrli, J.L. Williams, S.D. Kugelmass, Relationship between NMR transverse relaxation trabecular bone architecture and strength, Proc. Natl. Acad. Sci., U.S.A. 90 (1993) 10250–10254.
[15] D.A. Yablonskiy, W.R. Reinus, E.M. Haacke, H. Stark, Quantitation of T_2' anisotropic effects on MR bone mineral density measurement, Magn. Reson. Med. 37 (1996) 214–221.
[16] F.W. Wehrli, H.K. Song, P.K. Saha, A.C. Wright, Quantitative MRI for the assessment of bone structure and function, NMR Biomed. 19 (2006) 731–764.
[17] T.M. Link, S. Majumdar, P. Augat, J.C. Lin, D. Newitt, N.E. Lane, H.K. Genant, Proximal femur: assessment for osteoporosis with T_2^* decay characteristics at MR imaging, Radiology 209 (1998) 531–536.
[18] E.E. Sigmund, H. Cho, P. Chen, S. Byrnes, Y.Q. Song, X.E. Guo, T.R. Brown, Diffusion-based MR methods for bone structure and evolution, Magn. Reson. Med. 59 (2008) 28–39.
[19] E.E. Sigmund, H. Cho, Y.Q. Song, High-resolution MRI of internal field diffusion-weighting in trabecular bone, NMR Biomed. 22 (2009) 436–448.
[20] Y.Q. Song, S.G. Ryu, P.N. Sen, Determining multiple length scales in rocks, Nature 406 (2000) 178–181.
[21] N.V. Lisitza, Y.Q. Song, The behavior of diffusion eigenmodes in the presence of internal magnetic field in porous media, J. Chem. Phys. 114 (2001) 9120–9124.
[22] V. Bousson, C. Bergot, A. Meunier, F. Barbot, C. Parlier-Cuau, A.M. Laval-Jeantet, J.D. Laredo, CT of the middiaphyseal femur: cortical bone mineral density and relation to porosity, Radiology 217 (2000) 179–187.
[23] K.L. Bell, N. Loveridge, G.R. Jordan, J. Power, C.R. Constant, J. Reeve, A novel mechanism for induction of increased cortical porosity in cases of intracapsular hip fracture, Bone 27 (2000) 297–304.
[24] R.W. McCalden, J.A. McGeough, M.B. Barker, C.M. Court-Brown, Age-related changes in the tensile properties of cortical bone. The relative importance of changes in porosity, mineralization, and microstructure, J. Bone Joint Surg. Am. 75 (1993) 1193–1205.
[25] M.D. Robson, P.D. Gatehouse, M. Bydder, G.M. Bydder, Magnetic resonance. an introduction to ultrashort TE (UTE) imaging, J. Comput. Assist. Tomogr. 27 (2003) 825–846.
[26] A. Techawiboonwong, H.K. Song, F.W. Wehrli, In vivo MRI of submillisecond T(2) species with two-dimensional and three-dimensional radial sequences and applications to the measurement of cortical bone water, NMR Biomed. 21 (2007) 59–70.
[27] M.D. Robson, G.M. Bydder, Clinical ultrashort echo time imaging of bone and other connective tissues, NMR Biomed. 19 (2006) 765–780.
[28] M. Fernandez-Seara, S.L. Wehrli, F.W. Wehrli, Diffusion of exchangeable water in cortical bone studied by nuclear magnetic resonance, Biophys. J. 82 (2002) 522–529.
[29] M. Fernandez-Seara, S.L. Wehrli, M. Takahashi, F.W. Wehrli, Water content measured by proton–deuteron exchange NMR predicts bone mineral density and mechanical properties, J. Bone Miner. Res. 19 (2004) 289–296.
[30] I.L. Reichert, M.D. Robson, P.D. Gatehouse, T. He, K.E. Chappell, J. Holmes, S. Girgis, G.M. Bydder, Magnetic resonance imaging of cortical bone with ultrashort TE pulse sequences, Magn. Reson. Imaging 23 (2005) 611–618.
[31] A. Techawiboonwong, H.K. Song, M.B. Leonard, F.W. Wehrli, Cortical bone water: in vivo quantification with ultrashort echo-time MR imaging, Radiology 248 (2008) 824–833.
[32] R.A. Horch, J.S. Nyman, D.F. Gochberg, R.D. Dortch, M.D. Does, Characterization of 1H NMR signal in human cortical bone for magnetic resonance imaging, Magn. Reson. Med. 64 (2010) 680–687.
[33] P.T. Callaghan, C.H. Arns, P. Galvosas, M.W. Hunter, Y. Qiao, K.E. Washburn, Recent Fourier and Laplace perspectives for multidimensional NMR in porous media, Magn. Reson. Imaging 25 (2007) 441–444.
[34] H.H. Ong, A.C. Wright, F.W. Wehrli, Deuterium nuclear magnetic resonance unambiguously quantifies pore and collagen-bound water in cortical bone, J. Bone Miner. Res., 2012, http://dx.doi.org/10.1002 (July 13).
[35] C.L. Epstein, J. Schotland, The bad truth about Laplace's transform, Siam Rev. 50 (2008) 504–520.
[36] H. Shinar, G. Navon, Multinuclear NMR and microscopic MRI studies of the articular cartilage nanostructure, NMR Biomed. 19 (2006) 877–893.
[37] U. Eliav, G. Navon, A study of dipolar interactions and dynamic processes of water molecules in tendon by 1H and 2H homonuclear and heteronuclear multiple-quantum-filtered NMR spectroscopy, J. Magn. Reson. 137 (1999) 295–310.
[38] M.S. Sussman, J.M. Pauly, G.A. Wright, Design of practical T2-selective RF excitation (TELEX) pulses, Magn. Reson. Med. 40 (1998) 890–899.
[39] I.V. Mastikhin, B.J. Balcom, Centric SPRITE MRI of biomaterials with short T_2^*, in: Encyclopedia of Magnetic Resonance, John Wiley & Sons, Ltd., 2007.
[40] D. Idiyatullin, C. Corum, J.Y. Park, M. Garwood, Fast and quiet MRI using a swept radiofrequency, J. Magn. Reson. 181 (2006) 342–349.
[41] J.M. Pauly, Selective excitation for ultrashort echo time imaging, in: Encyclopedia of Magnetic Resonance, John Wiley & Sons, Ltd., 2012.
[42] F.W. Wehrli, Image-based assessment of cortical bone, in: Encyclopedia of Magnetic Resonance, John Wiley & Sons, Ltd., 2012.
[43] C.J. Bergin, J.M. Pauly, A. Macovski, Lung parenchyma: projection reconstruction MR imaging, Radiology 179 (1991) 777–781.
[44] A. Waldman, J.H. Rees, C.S. Brock, M.D. Robson, P.D. Gatehouse, G.M. Bydder, MRI of the brain with ultra-short echo-time pulse sequences, Neuroradiology 45 (2003) 887–892.
[45] M.J. Wilhelm, H.H. Ong, S.L. Wehrli, C. Li, P.H. Tsai, D.B. Hackney, F.W. Wehrli, Direct magnetic resonance detection of myelin and prospects for quantitative imaging of myelin density, Proc. Natl. Acad. Sci., U.S.A. 109 (2012) 9605–9610.

[46] J. Pauly, C. Conolly, A. Macovski, Supression of long-T2 components for short T2 imaging, in: SMRM, 12th Annual Meeting, New York, 1992, p. 145.

[47] H.S. Rad, S.C. Lam, J.F. Magland, H. Ong, C. Li, H.K. Song, J. Love, F.W. Wehrli, Quantifying cortical bone water in vivo by three-dimensional ultra-short echo-time MRI, NMR Biomed. 24 (2011) 855–864.

[48] M. Weiger, K.P. Pruessmann, A.K. Bracher, S. Kohler, V. Lehmann, U. Wolfram, F. Hennel, V. Rasche, High-resolution ZTE imaging of human teeth, NMR Biomed. 25 (2012) 1144–1151.

[49] M. Weiger, K.P. Pruessmann, F. Hennel, MRI with zero echo time: hard versus sweep pulse excitation, Magn. Reson. Med. 66 (2011) 379–389.

[50] Y. Wu, G. Dai, J.L. Ackerman, M.I. Hrovat, M.J. Glimcher, B.D. Snyder, A. Nazarian, D.A. Chesler, Water- and fat-suppressed proton projection MRI (WASPI) of rat femur bone, Magn. Reson. Med. 57 (2007) 554–567.

[51] D.M. Grodzki, P.M. Jakob, B. Heismann, Ultrashort echo time imaging using pointwise encoding time reduction with radial acquisition (PETRA), Magn. Reson. Med. 67 (2012) 510–518.

[52] D.O. Kuethe, A. Caprihan, I.J. Lowe, D.P. Madio, H.M. Gach, Transforming NMR data despite missing points, J. Magn. Reson. 139 (1999) 18–25.

[53] A.K. Bracher, C. Hofmann, A. Bornstedt, S. Boujraf, E. Hell, J. Ulrici, A. Spahr, B. Haller, V. Rasche, Feasibility of ultra-short echo time (UTE) magnetic resonance imaging for identification of carious lesions, Magn. Reson. Med. 66 (2011) 538–545.

[54] C. Li, J.F. Magland, H.S. Rad, H.K. Song, F.W. Wehrli, Comparison of optimized soft-tissue suppression schemes for ultrashort echo time MRI, Magn. Reson. Med. 68 (2011) 680–689.

[55] J. Du, A.M. Takahashi, W.C. Bae, C.B. Chung, G.M. Bydder, Dual inversion recovery, ultrashort echo time (DIR UTE) imaging: creating high contrast for short-T(2) species, Magn. Reson. Med. 63 (2010) 447–455.

[56] R. Biswas, W. Bae, E. Diaz, K. Masuda, C.B. Chung, G.M. Bydder, J. Du, Ultrashort echo time (UTE) imaging with bi-component analysis: bound and free water evaluation of bovine cortical bone subject to sequential drying, Bone 50 (2012) 749–755.

[57] J. Du, J.C. Hermida, E. Diaz, J. Corbeil, R. Znamirowski, D.D. D'Lima, G.M. Bydder, Assessment of cortical bone with clinical and ultrashort echo time sequences, Magn. Reson. Med. (2012).

[58] E. Diaz, C.B. Chung, W.C. Bae, S. Statum, R. Znamirowski, G.M. Bydder, J. Du, Ultrashort echo time spectroscopic imaging (UTESI): an efficient method for quantifying bound and free water, NMR Biomed. 25 (2012) 161–168.

[59] W.C. Bae, P.C. Chen, C.B. Chung, K. Masuda, D. D'Lima, J. Du, Quantitative ultrashort echo time (UTE) MRI of human cortical bone: correlation with porosity and biomechanical properties, J. Bone Miner. Res. 27 (2012) 848–857.

[60] R.A. Horch, D.F. Gochberg, J.S. Nyman, M.D. Does, Clinically compatible MRI strategies for discriminating bound and pore water in cortical bone, Magn. Reson. Med., 2012, http://dx.doi.org/10.1002 (January 31).

[61] R. Salomir, B.D. De Senneville, C.T.W. Moonen, A fast calculation method for magnetic field inhomogeneity due to an arbitrary distribution of bulk susceptibility, Concep. Magn. Reson. Part B 19B (2003) 26–34.

[62] X. Wang, Q. Ni, Determination of cortical bone porosity and pore size distribution using a low field pulsed NMR approach, J. Orthop. Res. 21 (2003) 312–319.

[63] Y. Wu, J.L. Ackerman, D.A. Chesler, L. Graham, Y. Wang, M.J. Glimcher, Density of organic matrix of native mineralized bone measured by water- and fat-suppressed proton projection MRI, Magn. Reson. Med. 50 (2003) 59–68.

[64] G.Y. Boivin, P.M. Chavassieux, A.C. Santora, J. Yates, P.J. Meunier, Alendronate increases bone strength by increasing the mean degree of mineralization of bone tissue in osteoporotic women, Bone 27 (2000) 687–694.

[65] H. Cao, J.L. Ackerman, M.I. Hrovat, L. Graham, M.J. Glimcher, Y. Wu, Quantitative bone matrix density measurement by water- and fat-suppressed proton projection MRI (WASPI) with polymer calibration phantoms, Magn. Reson. Med. 60 (2008) 1433–1443.

[66] Y. Wu, D.A. Chesler, M.J. Glimcher, L. Garrido, J. Wang, H.J. Jiang, J.L. Ackerman, Multinuclear solid-state three-dimensional MRI of bone and synthetic calcium phosphates, Proc. Natl. Acad. Sci. U.S.A. 96 (1999) 1574–1578.

[67] A.C. Seifert, A.C. Wright, H.H. Ong, T.J. Connick, S. Pickup, S.L. Wehrli, F.W. Wehrli, Magnetic field dependence of 31P relaxation in cortical bone, in: Proc. ISMRM, Melbourne, Australia, 2012, p. 1414.

[68] S. Anumula, J. Magland, S.L. Wehrli, H. Zhang, H. Ong, H.K. Song, F.W. Wehrli, Measurement of phosphorus content in normal and osteomalacic rabbit bone by solid-state 3D radial imaging, Magn. Reson. Med. 56 (2006) 946–952.

[69] S. Anumula, S.L. Wehrli, J. Magland, A.C. Wright, F.W. Wehrli, Ultra-short echo-time MRI detects changes in bone mineralization and water content in OVX rat bone in response to alendronate treatment, Bone 46 (2010) 1391–1399.

[70] Y. Wu, M.J. Glimcher, C. Rey, J.L. Ackerman, A unique protonated phosphate group in bone mineral not present in synthetic calcium phosphates. Identification by phosphorus-31 solid state NMR spectroscopy, J. Mol. Biol. 244 (1994) 423–435.

[71] Y. Wu, T.G. Reese, H. Cao, M.I. Hrovat, S.P. Toddes, R.A. Lemdiasov, J.L. Ackerman, Bone mineral imaged in vivo by (31) P solid state MRI of human wrists, J. Magn. Reson. Imaging 34 (2011) 623–633.

[72] M.J. Wald, J.F. Magland, C.S. Rajapakse, F.W. Wehrli, Structural and mechanical parameters of trabecular bone estimated from in vivo high-resolution magnetic resonance images at 3 tesla field strength, J. Magn. Reson. Imaging 31 (2010) 1157–1168.

[73] F.W. Wehrli, Structural and functional assessment of trabecular and cortical bone by micro magnetic resonance imaging, J. Magn. Reson. Imaging 25 (2007) 390–409.

[74] T.M. Link, Osteoporosis imaging: state of the art and advanced imaging, Radiology 263 (2012) 3–17.

[75] G.A. Ladinsky, B. Vasilic, A.M. Popescu, M. Wald, B.S. Zemel, P.J. Snyder, L. Loh, H.K. Song, P.K. Saha, A.C. Wright, F.W. Wehrli, Trabecular structure quantified with the MRI-based virtual bone biopsy in postmenopausal women contributes to vertebral deformity burden independent of areal vertebral BMD, J. Bone Miner. Res. 23 (2008) 64–74.

[76] T. Hildebrand, A. Laib, R. Muller, J. Dequeker, P. Ruegsegger, Direct three-dimensional morphometric analysis of human cancellous bone: microstructural data from spine, femur, iliac crest, and calcaneus, J. Bone Miner. Res. 14 (1999) 1167–1174.

[77] X.S. Liu, P. Sajda, P.K. Saha, F.W. Wehrli, X.E. Guo, Quantification of the roles of trabecular microarchitecture and trabecular type in determining the elastic modulus of human trabecular bone, J. Bone Miner. Res. 21 (2006) 1608–1617.

[78] T.P. Harrigan, R.W. Mann, Characterization of microstructural anisotropy in orthotropic materials using a second rank tensor, J. Mater. Sci. 19 (1984) 761–767.

[79] S.N. Hwang, F.W. Wehrli, J.L. Williams, Probability-based structural parameters from 3D NMR images as predictors of trabecular bone strength, Med. Phys. 24 (1997) 1255–1261.

[80] M.J. Wald, B. Vasilic, P.K. Saha, F.W. Wehrli, Spatial autocorrelation and mean intercept length analysis of trabecular bone anisotropy applied to in vivo magnetic resonance imaging, Med. Phys. 34 (2007) 1110–1120.

[81] M.J. Wald, J.F. Magland, C.S. Rajapakse, Y.A. Bhagat, F.W. Wehrli, Predicting trabecular bone elastic properties from measures of bone volume fraction and fabric on the basis of micromagnetic resonance images, Magn. Reson. Med. 68 (2012) 463–473.

[82] B. Van Rietbergen, A. Odgaard, J. Kabel, R. Huiskes, Direct mechanics assessment of elastic symmetries and properties of trabecular bone architecture, J. Biomech. 29 (1996) 1653–1657.

[83] J.F. Magland, N. Zhang, C.S. Rajapakse, F.W. Wehrli, Computationally-optimized bone mechanical modeling from high-resolution structural images, PLoS ONE 7 (2012) e35525.

[84] J. Kabel, B. van Rietbergen, M. Dalstra, A. Odgaard, R. Huiskes, The role of an effective isotropic tissue modulus in the elastic properties of cancellous bone, J. Biomech. 32 (1999) 673–680.

[85] C.S. Rajapakse, J.F. Magland, M.J. Wald, X.S. Liu, X.H. Zhang, X.E. Guo, F.W. Wehrli, Computational biomechanics of the distal tibia from high-resolution MR and micro-CT images, Bone 47 (2010) 556–563.

[86] C.S. Rajapakse, M.B. Leonard, Y.A. Bhagat, W. Sun, J.F. Magland, F.W. Wehrli, Micro-MR imaging-based computational biomechanics demonstrates reduction in cortical and trabecular bone strength after renal transplantation, Radiology 262 (2012) 912–920.

[87] X.H. Zhang, X.S. Liu, B. Vasilic, F.W. Wehrli, M. Benito, C.S. Rajapakse, P.J. Snyder, X.E. Guo, In vivo microMRI-based finite element and morphological analyses of tibial trabecular bone in eugonadal and hypogonadal men before and after testosterone treatment, J. Bone Miner. Res. 23 (2008) 1426–1434.

[88] F.W. Wehrli, C.S. Rajapakse, J.F. Magland, P.J. Snyder, Mechanical implications of estrogen supplementation in early postmenopausal women, J. Bone Miner. Res. 25 (2010) 1406–1414.

[89] N. Zhang, J. Magland, C. Rajapakse, Y. Bhagat, S.C. Lam, F.W. Werhli, Linear and nonlinear high-resolution finite-element analysis of the distal tibia and radius from in vivo MRI, in: ASBMR 2012 Annual Meeting, J. Bone Miner. Res., Minneapolis, MN, 2012.